

Article pubs.acs.org/JPCC

# Performance of Transparent Metallic Thin Films

Yanfeng Wang, Fei Yang, Zhengjun Zhang,\* and Yiping Zhao\*



Cite This: J. Phys. Chem. C 2021, 125, 16334-16342



**ACCESS** I

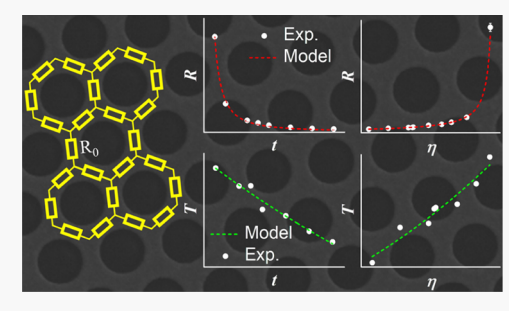
Metrics & More



Article Recommendations

Supporting Information

ABSTRACT: The ability to maintain high electrical conductivity and optical transparency simultaneously under mechanical deformation has made transparent metallic films (TMFs) the best candidates among transparent conductive films (TCFs). However, there is a lack of suitable models to predict the overall performance of the TMFs. Here, empirical relationships for resistance  $R_s$  based on the network resistor model, Kirchoff's rules, and the thickness-dependent resistivity and transmission T based on the effective medium theory, the geometric model, and the Beer-Lambert law are proposed. A systematic thickness t- and perforation area ratio PR-dependent study on the silver nanohole array TMF has been performed. Both models fit well with our experimental data as well as the data reported in the literature, regardless of the lattice structure of the TMFs. A general



and comprehensive figure-of-merit (FOM) expression for TMFs,  $\Phi = T^{\beta}/R_s$ , is obtained. Both the experimental data and the theoretical predictions show that  $\beta = 5$  is better to characterize the performance of nanohole array TMFs as compared to  $\beta = 10$  for TCFs. The observed empirical models and the FOM expression not only can be used to assess the overall quality of any type of TMFs but also provide guidance for fabrication.

#### INTRODUCTION

The increasing interest in developing high-performance and low-cost flexible optoelectronic devices has led to intense research activities on transparent metallic films (TMFs), which enable electrical conductivity and optical transparency simultaneously under mechanical deformation. In general, TMFs are perforated thin metallic networks with nano- and/or microstructures.<sup>2</sup> There are two forms of TMFs, the porous metal thin films and the percolated metal nanowire (NW) network. The connectivity of the metal network guarantees good conductivity, while the porosity allows light to transmit through to achieve high transparency. Efforts have been dedicated to improve the transmittance and electrical conductivity of TMFs by adjusting the thickness,<sup>3,4</sup> size,<sup>5</sup> and/or periodicity<sup>4</sup> of the quasi-2D porous structure as well as using different metallic materials.<sup>4,6</sup>

For a TMF, the sheet resistance  $R_s$  and transmission T are two most important parameters to characterize its performance and both are mainly determined by the thickness t and porosity or perforation area ratio PR (PR =  $1 - A_m/A_0$ , where  $A_0$  is the total area of the film and  $A_m$  is the metal covered area) of the structure. However, the t and PR have a different influence on  $R_s$  and T.  $R_s$  of a TMF is inversely proportional to t,  $R_s = \rho t^{-1}$ , but positively associated with PR. In addition, the intrinsic resistivity  $\rho$  of the film or NW network also depends on t and the quality of the film/NW. If t is close to the mean free path  $l_{\rm M}$  of the electron in the metal, surface/interface scattering can contribute significantly to  $\rho$ ; thus,  $\rho$  can increase significantly with the decrease of t.8 Similarly, the quality of the thin film, such as surface roughness and grain boundaries, has a considerable influence on  $\rho$ . Similarly, the diameter, the smoothness of the NW as well as NW junctions, or surface modifications determine the corresponding  $\rho$ . However, in most TMF modeling works on  $R_{s}$ , people did not consider these effects. For example, Reilly and Tenent established a resistance model based on the percolation theory to study the relationship between R<sub>s</sub> and PR of the metallic nanohole (MNH) array with  $R_s = A \cdot (PR_{crit} - PR)^x$ , where A is the preexponential factor, PR<sub>crit</sub> is the critical nanohole coverage condition where the probability of a conducting pathway in the film falls to 0, and x is the 2D conductivity exponent.<sup>11</sup> However, the model is only applicable to the randomly distributed MNH structure. Li et al. believed that  $R_s$  increased linearly with the increase of diameter of the NH, which is contradictory to most of the current work on the square metal NW network.  $^{3,12}$  For the 2D square metal NW network with N $\times$  N wires,  $R_{\rm s}$  was calculated directly according to Kirchhoff's rules,  $R_s = \frac{N}{N+1} \frac{\rho L}{tW} \approx \frac{\rho L}{tW}$ , where L is the spacing of the NW and W is the width of the NW.<sup>3,12</sup>

Similar to  $R_s$ , the T of a TMF is also closely related to t, PR, and the quality of the film/network. In general, the skin depth  $\delta$  of a metal  $(\delta=\sqrt{\frac{2\rho}{\omega\mu_0\mu_{\rm f}}})$  and the Beer–Lambert law give the

Received: June 1, 2021 Revised: July 3, 2021 Published: July 19, 2021





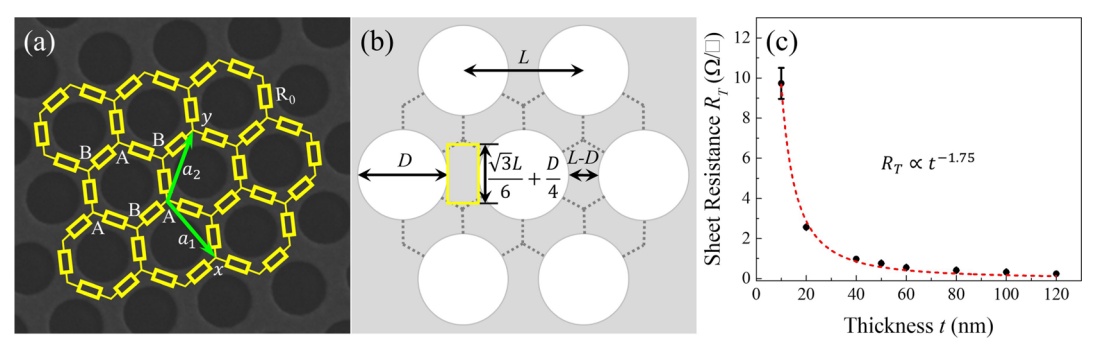


**Figure 1.** (a) Schematic of the infinite two-dimensional hexagonal lattice of identical resistors  $R_0$ . (b) Schematic of the unit resistor  $R_0$ . (c) Power law fitting of the sheet resistance  $R_{\rm T}$  vs thickness t for continuous Ag thin films.

t-dependent transmission ( $T \propto e^{-\alpha t}$ ), where the optical absorption coefficient  $\alpha = \frac{2}{s}$ . The PR governs the effective dielectric function  $\varepsilon_{\rm eff}$  of the TMF. If 1 - PR is close to 0, according to the Maxwell-Garnett approximation,  $\varepsilon_{\mathrm{eff}} \approx (1 -$ PR) $\cdot \varepsilon_{\rm m}$  + PR $\cdot \varepsilon_{\rm Air}$ , where  $\varepsilon_{\rm Air}$  and  $\varepsilon_{\rm m}$  are the dielectric functions of air and metal, respectively. 13 The thickness of the metal film or the spacing and width of the NW determine the intrinsic transmission and extinction property of the structure. However, many structures used in TMFs are also composed of subwavelength holes or even hole arrays, such as the NH array fabricated by nanosphere lithography (NSL), with a strong plasmonic effect; in particular, the extraordinary optical transmission (EOT) effect will occur. 14,15 In this case, both the Beer-Lambert law and effective medium theory are not valid, rather the surface plasmonic waves and the localized surface plasmon resonance (SPR) dominate the transmission property. In addition, the quality of the film or NW has a significant effect on the optical property of the structure since the skin depth  $\delta$  is proportional to  $\sqrt{\rho}$ . Numerical analysis methods such as finite difference time domain (FDTD) methods<sup>7,16</sup> and finite element methods (FEMs) $^{1,4}$  are used to predict  $R_s$  and Tof TMFs. These methods are effective for regularly spaced MNHs; however, they are time-consuming and computationally expensive.

Clearly, for a high-performance TMF, it is desired that  $R_s$  be as small as possible while T be close to 1. The small  $R_s$  requires a thicker and less porous film, while the large T imposes that tshall be small and PR should be close to 1. These two requirements result in a contradictory. Thus, to obtain a good TMF, compromise is needed for the values of  $R_s$  and T. To assess the performance of a TMF, a figure of merit (FOM),  $\Phi_{\rm H}$ =  $T^{\beta}/R_{s}$ , called the "Haacke" number, has been suggested by Haacke, where  $\beta$  is an exponent.<sup>17</sup> Originally, the  $\Phi_{\rm H}$  was proposed to characterize the performance of continuous transparent conductive films (TCFs) such as indium tin oxide thin films, of which T follows the Beer-Lambert law, T  $\propto e^{-\alpha t}$ , and  $R_s$  scales inversely with thickness,  $R_s = \rho t^{-1}$ , so that  $\Phi_{\rm H} \propto t {\rm e}^{-\alpha\beta t} \, \rho^{-1.17}$  For the traditional continuous TCFs, the  $\beta$ was chosen to be equal to 10 so that  $T\sim 90\%$  when  $\Phi_{\rm H}$ reaches its maximum, while few transparent conductor applications require more than 90% transmission. 17 Currently, for the TMFs, many works still use the same  $\beta = 10$  to evaluate the FOM. 18-21 However, due to the influence of surface roughness and grain boundaries, the porosity of the TMFs, and the EOT effect, the relationships,  $R_s \propto t^{-1}$  and  $T \propto e^{-\alpha t}$ , are not always satisfied. Thus,  $\Phi_H$  with  $\beta = 10$  is not necessarily the best parameter to evaluate the performance of the TMFs.

Either a case-by-case analysis or a systematic study is needed to obtain the best exponent  $\beta$  for TMFs.

In this work, we have systematically varied t and PR of the hexagonally arranged Ag NH array and investigated the corresponding transmission and sheet resistance both experimentally and theoretically. A general expression of  $R_{\rm s}$  and T as a function of t and D/L, where D is the diameter of the NH and L is the periodicity of the NH array, is obtained, and the relationships fit very well with our experimental data as well as the results from various literature studies. Based on the experimental results as well as the two empirical expressions, a comprehensive  $\Phi_{\rm H}$  expression with  $\beta \approx 5$  is proposed for TMFs.

# **EXPERIMENTAL SECTION**

**Materials.** Polystyrene nanospheres (PSNSs) with diameters of 500 and 750 nm (polyscience, Lot# 679675 and Lot# 687640) and ethanol (Sigma-Aldrich, 98%) were used to form the nanosphere monolayers on cleaned glass slides (Gold Seal, Part# 3010). Sulfuric acid (Fisher Scientific, 98%), ammonium hydroxide (Fisher Scientific, 98%), and hydrogen peroxide (Fisher Scientific, 30%) were used to clean the substrates. Silver (Trillion Metals Co., Ltd., 99.99%) and titanium pellets [Zhongnuo Advanced Material (Beijing) Technology Co., 99.995%] were purchased as the evaporation materials. Deionized water (18 MΩ cm) was used throughout the experiments. All chemicals and materials were used without further purification.

Fabrication of Ag NH. The fabrication process of NH utilized NSL and the shadowing growth technique. 22-25 A hexagonally close-packed monolayer of PSNS with an initial diameter of L = 500 or 750 nm was prepared on glass substrates by an air-water interface method. The procedure was described in detail in several previous publications. 26-28 The size of the PSNS on the substrates was shrunk to a smaller diameter D via reactive ion etching (RIE, L-451D-L, ANELVA) with varied etching times. The etched PSNS monolayer-coated substrates were loaded into a custom-built electron-beam deposition system and mounted on a substrate holder. The vacuum chamber was pumped down under a base pressure of <10<sup>-6</sup> Torr, and the PSNS monolayer-coated substrates were positioned to face normal to the vapor deposition direction. All the deposition thicknesses and rates were monitored using a quartz crystal microbalance facing the source. First, 3 nm thick Ti was deposited to promote the adhesion of the subsequent Ag layer. Then, the Ag layer with different thicknesses was deposited at a deposition rate of 0.05 nm/s to form the NH structure. After the Ag deposition, the PSNS monolayer was removed using Scotch tape.

Morphological, Optical, and Electrical Characterizations. The morphology of the resultant MNH structures was characterized by field-emission scanning electron microscopy (Zeiss GeminiSEM 500). The SEM images were analyzed by the ImageJ software (NIH). The sheet resistances of the Ag NH arrays were measured by a four-point probe method (4 Dimensions Inc., 280SJ). The optical transmission spectra of the structures were characterized using an ultraviolet—visible spectrophotometer (Perkin Elmer Lambda 35).

Numerical Calculations. A commercial software package (Ansys Lumerical 2020 R2 Finite Difference IDE) was used to calculate the transmission spectra of the Ag NH structures. A unit cell was set as the calculation area with periodic boundary conditions in the two lateral dimensions. Perfectly matched layer boundary conditions were used on the top and bottom surfaces of the calculation domain. Monitors of "frequency-domain field and power" were set up to determine the transmission spectra. The optical parameters for Ag and the glass (SiO<sub>2</sub>) substrate were taken from Palik's handbook.<sup>29</sup>

# RESULTS AND DISCUSSION

can be calculated as

Resistor and Transmission Models for TMF. For a hexagonal MNH structure shown in Figure 1a, it can be treated as an infinite honeycomb resistor network of identical unit resistors (the yellow squares shown in Figure 1a,b) with a resistance of  $R_0$ . Based on Ohm's law and the geometric relationship in the hexagonal lattice, the resistance  $R_0$  can be expressed as  $R_0 = \rho \cdot \frac{l}{w \cdot t} = \rho \cdot \frac{\sqrt{3}}{(1-\eta) \cdot t}$ , where  $\eta = D/L$ . Details are shown in Figure S1 in the Supporting Information. Based on the work by Atkinson and van Steenwijk<sup>30</sup> and Cserti,<sup>31</sup> the resistance  $R_{\rm NH}$  between the origin (0,0) and a given lattice point (m,n) of a two-dimensional hexagonal resistor network

$$R_{\rm NH} = K \cdot R_0 = K \cdot \rho \cdot \frac{\frac{\sqrt{3}}{6} + \frac{1}{4}\eta}{(1 - \eta) \cdot t}$$
 (1)

where  $K=\frac{3}{4\pi^2}\int_{-\pi}^{\pi}\int_{-\pi}^{\pi}\frac{1-\cos(mx+ny)}{3-\cos x-\cos y-\cos(x+y)}\mathrm{d}x\mathrm{d}y$ . For a tetragonal MNH structure shown in Figure S2 of the Supporting Information, a similar expression,  $R_{\mathrm{NH}}=K\cdot R_0=K\cdot \rho\cdot \frac{\frac{1}{2}+\frac{\sqrt{2}}{4}\eta}{(1-\eta)\cdot t}$ , is obtained, with  $K=\frac{1}{4\pi^2}\int_{-\pi}^{\pi}\int_{-\pi}^{\pi}\frac{1-\cos(mx+ny)}{2-\cos x-\cos y}\mathrm{d}x\mathrm{d}y$ .  $^{30,31}$  Therefore, it is expected that a general expression for the resistance R versus  $\eta$  for any TMFs can be written as

$$R = \frac{K \cdot \rho}{t} \cdot \frac{a + \eta}{b - \eta} \tag{2}$$

where a and b are unitless factors determined by the lattice symmetry. Thus, for TMFs, the sheet resistance  $R_s = \frac{K' \cdot \rho}{t} \cdot \frac{a + \eta}{b - \eta}$  is supposed to be inversely proportional to t. However, when the film thickness t is close to the electronic mean free path  $l_{\rm M}$  of a metal or the quality of the film is poor, the resistivity  $\rho$  is no longer a constant equal to the bulk resistivity  $\rho_0$ . In fact,  $\rho$  depends on the film thickness, the surface roughness, and the grain boundary of the metallic thin film and increases nonlinearly with the decrease of t, as explained by the F u c h s - S o n d h e i m e r the e o r y,  $\frac{3}{3}$  as  $\frac{3}{3}$ 

$$\rho = \rho_0 \bigg[ 1 - \frac{3}{2\kappa} (1-p) \int_0^1 (t-t^3) \frac{1-\mathrm{e}^{-\kappa/t}}{1-p\mathrm{e}^{-\kappa/t}} \mathrm{d}t \bigg]^{-1}, \qquad \text{w h e r e}$$
 
$$\kappa = t/l_{\mathrm{M}} \quad \text{and } p \quad \text{is the probability that an electron will be}$$
 specularly reflected upon scattering from one of the surfaces. Typical values for  $p$  are 0 for polycrystalline films and 0.5 for single-crystal films. Characteristics such as roughness can be considered to be included in parameter  $p$  since they directly affect the way electrons are scattered. We have performed a systematic experiment to measure the sheet resistance  $R_{\mathrm{T}}$  of the e-beam evaporated Ag thin film as a function of  $t$ , as shown

the e-beam evaporated Ag thin film as a function of t, as shown in Figure 1c. The  $R_{\rm T}$  increases as a power law of t,  $R_{\rm T} \propto t^{\gamma}$ , with  $\gamma = -1.75 \pm 0.07$ . Therefore, for an arbitrary TMF, the general relationship for the sheet resistance  $R_{\rm s}$ , t, and  $\eta$  can be adjusted to

$$R_{\rm s} = K' \cdot \frac{a + \eta}{b - \eta} \cdot t^{\gamma} \tag{3}$$

Here,  $R_{\rm T} = aK't'/b$  represents the sheet resistance of the corresponding thin film with the same t when  $D \to 0$  ( $\eta \to 0$ ).

The transmission model is also important for providing guidance for the exploration of high-quality TMFs. For the TMFs with different structures, T is related to the structure, that is, the diameter, periodicity, and the arrangement of the perforated apertures. Based on the effective medium theory, the effective dielectric function of the thin film  $\varepsilon_{\rm eff} \approx \varepsilon_{\rm Ag} + {\rm PR} \cdot (\varepsilon_{\rm Air} - \varepsilon_{\rm Ag})$ , where  ${\rm PR} = A_0 \eta^2$  and  $A_0$  is a shape factor. Also, according to the Fresnel equations,  $T = 1 - \left(\frac{n_{\rm eff}-1}{n_{\rm eff}+1}\right)^2$ , where  $n_{\rm eff} = \sqrt{\varepsilon_{\rm eff}}$ . Thus, in the limit where PR is close to 1,

$$\begin{split} T(P\vec{R}1) &\approx 1 - \left(\frac{\sqrt{\varepsilon_{Air}} - 1}{\sqrt{\varepsilon_{Air}} + 1}\right)^2 - \frac{2(\varepsilon_{Air} - \varepsilon_{Ag})}{\sqrt{\varepsilon_{Air}}} \\ &\cdot \frac{\sqrt{\varepsilon_{Air}} - 1}{\left(\sqrt{\varepsilon_{Air}} + 1\right)^3} \cdot (PR - 1) \end{split}$$

$$T(\vec{PR1}) \approx \left[1 - \left(\frac{\sqrt{\varepsilon_{Air}} - 1}{\sqrt{\varepsilon_{Air}} + 1}\right)^2 + \frac{2(\varepsilon_{Air} - \varepsilon_{Ag})}{\sqrt{\varepsilon_{Air}}}\right] \cdot \frac{\sqrt{\varepsilon_{Air}} - 1}{(\sqrt{\varepsilon_{Air}} + 1)^3} + \frac{2(\varepsilon_{Ag} - \varepsilon_{Air})}{\sqrt{\varepsilon_{Air}}} v_s^2 \frac{\sqrt{\varepsilon_{Air}} - 1}{(\sqrt{\varepsilon_{Air}} + 1)^3} \cdot A_s n^2$$

$$(4)$$

Thus, when the PR is very close to 1, the relationship between T and the ratio  $\eta$  can be approximated by the following equation:

$$T = A\eta^2 + B \tag{5}$$

where A and B are the corresponding expressions determined in eq 4. This equation is, in fact, consistent with the equation proposed based on simple geometric models in many studies. For the geometric model, the apertures are assumed to be 100% transmission and the metal areas are believed to be 100% reflection. In Ignoring surface plasmon absorption, the percent transmission follows  $T = 100\% \times PR$ . However, for a thin metal film, the transmission should be larger than 0. For example, Figure S3 in the Supporting Information shows the transmission spectra  $T(\lambda)$  of Ag thin films with different t (10–120 nm). In addition, for TMFs with ordered NH structures, the transmission efficiency through the

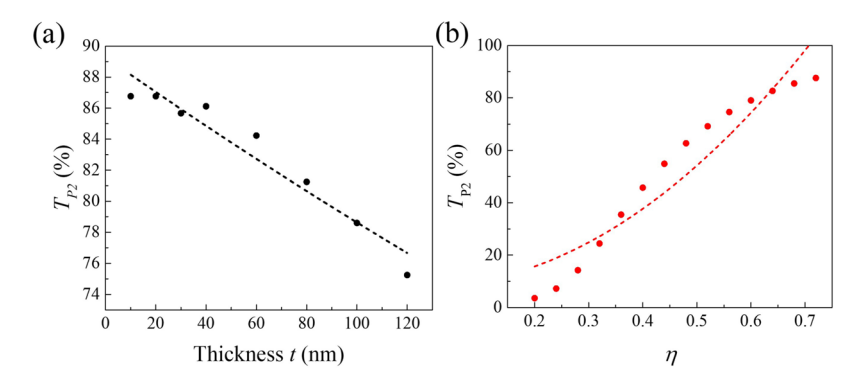


**Figure 2.** (a) Plot of  $T_{P_2}$  (indicated in Figure S4) extracted from FDTD-calculated  $T(\lambda)$  for Ag NH with different t, L=500 nm, and D=340 nm. (b) Plot of  $T_{P_2}$  extracted from FDTD-calculated  $T(\lambda)$  for Ag NH with different  $\eta$ , L=500 nm, and t=50 nm.

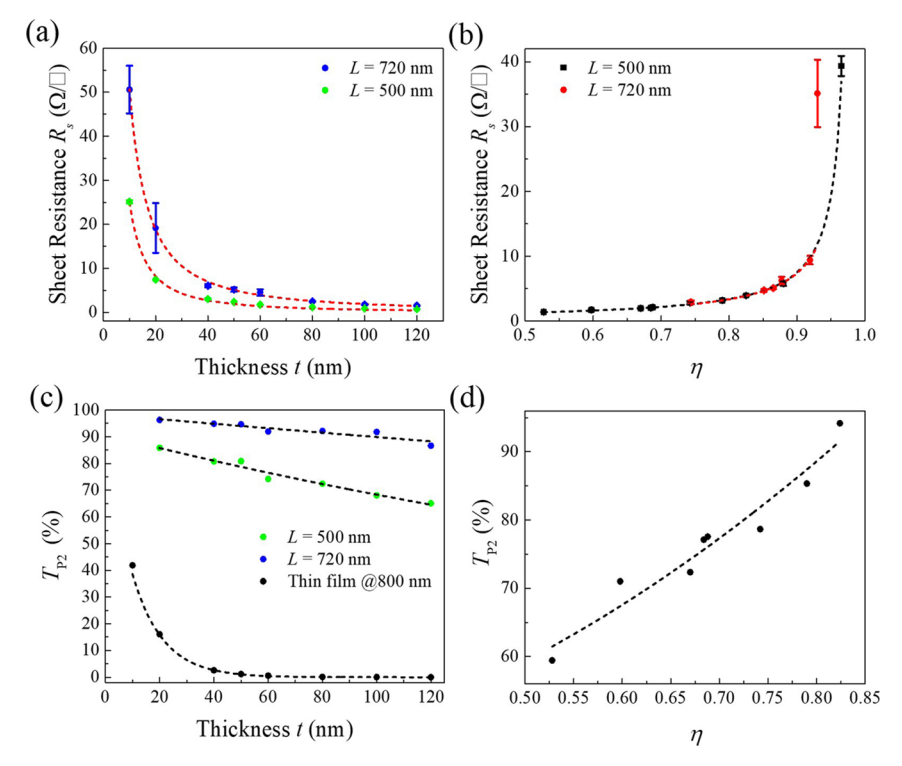


Figure 3. (a) Plot of  $R_s$  vs t for Ag MNHs (L=500 nm, D=344 nm and L=720 nm, D=613 nm). (b) Plot of  $R_s$  vs  $\eta$  for Ag MNH (L=500 nm and L=720 nm) with a fixed t=50 nm. (c) Plot of  $T_{P_2}$  vs t for Ag MNH (L=500 nm, D=344 nm and L=720 nm, D=613 nm). The transmission at  $\lambda=800$  nm for the Ag thin film with the same t is also shown in the figure. (d) Plot of  $T_{P_2}$  vs  $\eta$  for Ag MNH with L=500 nm.

apertures may be larger than 100% due to the EOT effect caused by the SPR  $^{35}$  Assuming that the light transmitted through the area of the apertures is  $T_{\rm A}$  and that through a Ag thin film with the same thickness are  $T_{\rm M}$  ( $T_{\rm A} > T_{\rm M} \geq 0$ ), the transmission of the TMFs follows an empirical equation:  $T=T_{\rm A} \times {\rm PR} + T_{\rm M} \times (1-{\rm PR}) = (T_{\rm A} - T_{\rm M}) \times {\rm PR} + T_{\rm M}$  with  ${\rm PR} = \frac{\pi \eta^2}{2\sqrt{3}}$  for the hexagonally arranged MNH structure and  ${\rm PR} = \frac{\pi \eta^2}{4}$  for the tetragonally arranged MNH structure. Clearly, such a result is similar to eq 5 but with  $T_{\rm A}$  close to 1 and  $T_{\rm M}$  close to 0.

However, eq 5 does not take the influence of t on T into account. Considering the Beer–Lambert law, eq 5 should be modified to

$$T = [A \cdot \eta^2 + B] \cdot e^{-\alpha t}$$
 (6)

Equation 6 is a general expression which can be used to study the transmittance of TMFs with different structures as well as thicknesses.

To test whether eq 6 is valid or not, we have carried out the FDTD calculations on ordered MNH to explore the T,  $\eta$ , and t relationships. The calculated transmission spectra  $T(\lambda)$  of hexagonal Ag NH with different t (L = 500 nm and D = 340 nm) and  $\eta$  (L = 500 nm and t = 50 nm) are shown in Figure S4 of the Supporting Information. When t or  $\eta$  is relatively large, the  $T(\lambda)$  spectra have two characteristic EOT peaks ( $P_1$  and  $P_2$ ) caused by the SPR at the air—Ag and the Ag—glass interfaces. However, with the decrease of t,  $P_2$  red-shifts, while the spectra shape changes from a sharp peak to a clear transmission dip. This is due to the weakening of SPR at the two interfaces and the enhancement of the dip mode. The dip mode is attributed to the short-range surface plasmon polaritons associated with the symmetric coupled mode

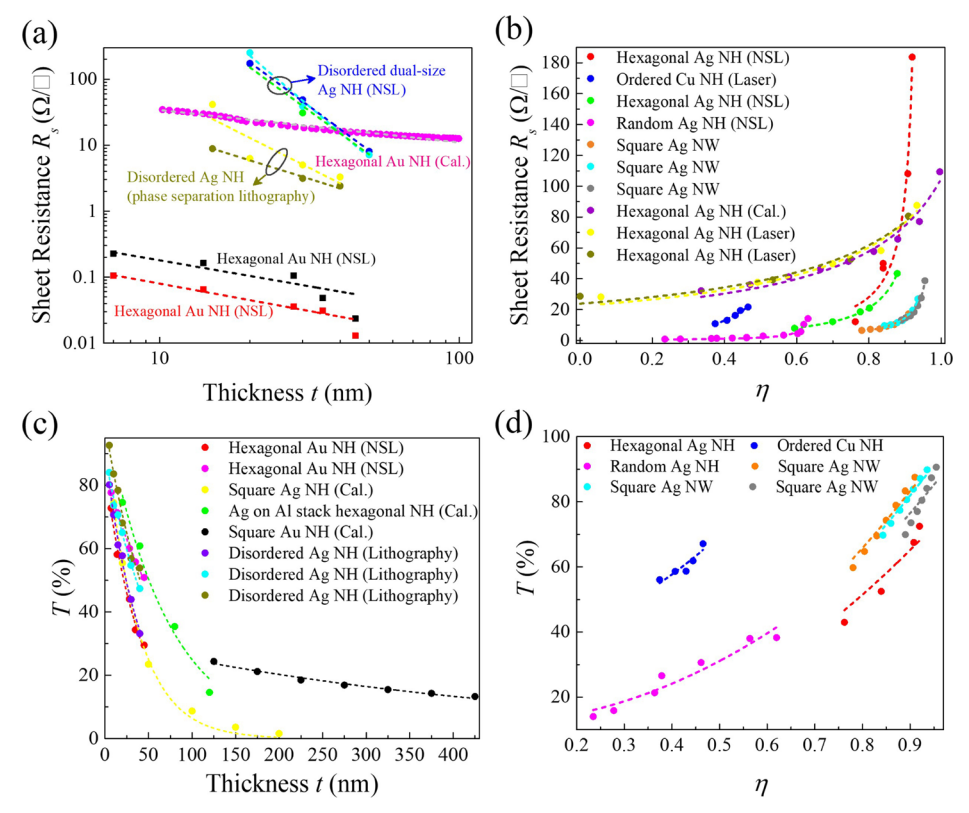


Figure 4. (a) R<sub>s</sub> vs t plots of various TMFs: (black and red squares) hexagonal Au NH fabricated by NSL<sub>1</sub><sup>37</sup> (pink dots) calculated hexagonal Au NH, (green, blue, and cyan dots) disordered dual-size Ag NH fabricated by NSL, 38 and (yellow and dark-yellow dots) disordered Ag NH fabricated by phase separation lithography.<sup>39</sup> (b)  $R_s$  vs  $\eta$  plots of various TMFs: hexagonal Ag NH fabricated by NSL, <sup>18</sup> laser-processed ordered Cu NH, hexagonal ordered Ag NH fabricated by NSL, random Ag NH fabricated by NSL, the square Ag NW network, and laser-perforated Ag NHs.  $^{34}$  (c) T vs t plots of various TMFs: hexagonal Au NH  $(T_{P_1})$  fabricated by NSL,  $^{37}$  the calculated square array of Ag NH  $(T_{P_2})$ ,  $^{36}$  calculated Ag on Al stack hexagonal ordered NH (T at  $\lambda = 900$  nm), the calculated square array of Au NH ( $T_P$ ), t=0.00 and disordered Ag NH fabricated by phase separation lithography (T at  $\lambda = 550$  nm).  $^{39}$  (d) T vs  $\eta$  plots of various TMFs: hexagonal Ag NH (average fractional transmission 350–1200 nm) fabricated by NSL, 18 laser-processed ordered Cu NH (T at  $\lambda = 550$  nm), 4 random Ag NH ( $T_{p_1}$ ) fabricated by NSL, 11 and the square Ag NW network (T at  $\lambda = 550$  nm). 12 The dashed curves are the fitting results based on eqs 3 and 6.

between the two interfaces.<sup>36</sup> The  $T_{P_3}$  for Ag NH with different t is plotted in Figure 2a. The black-dashed curves show the fitting result according to eq 6,  $T_{\rm FDTD}$  = 0.893 × e<sup>-0.0013×t</sup>. The mismatch between the fitting and experimental results in the area of smaller t is due to the disappearance of the EOT effect due to the weakening of SPR at the two interfaces.

With the increase of  $\eta$ , peak  $P_2$  red-shifts with the transmission of the resonance peaks and their spectral widths increase, as shown in Figure S4b of the Supporting Information. When  $\eta$  approaches 1, which means that D is very large and the MNH is close to an open area, the spectra shape changes from sharp peaks to a very broad peak which is determined mainly by the direct transmission without coupling with the discrete resonant state. This is because the effect of SPR at the two interfaces becomes less significant.<sup>36</sup> Figure 2b plots  $T_{P_2}$  versus  $\eta$ , and the dashed curve shows the fitting result according to eq 6. Overall, the proposed  $T-\eta$  relationship in eq 6 fits well with the FDTD results, with  $T_{\rm FDTD} = (1.99\eta^2 + 0.09) \times {\rm e}^{-0.0013\times 50}$ . The fitting parameter A (=1.99) is larger than 1, while B (=0.09) is close to 0. This satisfies the geometric model where A represents the over 100% transmission efficiency of the NH due to the EOT effect and B represents the near 0 transmittance through the metallic film. However, there exists mismatch between the fitting and experimental results in large  $\eta$ . Also, when  $\eta = 0.68$ , the

coefficient before the exponent is 1.01 for the fitting in Figure 2b, larger than the 0.893 obtained from the fitting for tdependence relationship in Figure 2a. This is due to the disappearance of the EOT effect when  $\eta$  approaches 1.

## SYSTEMATIC EXPERIMENTAL RESULTS

To experimentally validate the  $R_s$  and T relationship shown in egs 3 and 6, we have systematically fabricated various Ag MNH arrays with different t (from 10 to 120 nm), L (720 and 500 nm), and D. Figures S5 and S6 show some representative SEM images of Ag NH structures with different D and L. The  $R_s$  of the Ag NH structures with L = 500 nm, D = 344 nm and L = 720 nm, D = 613 nm of different t are plotted in Figure 3a and show a quick decrease with the increase of t. The best fitting result using eq 3 gives  $R_{720} = 1360 \times t^{-1.43} \Omega / \square (\eta = 0.85)$  and  $R_{500} = 1000 \times t^{-1.60} \Omega / \square (\eta = 0.69)$ . Regardless of the L and D, both sets of data give a similar exponent  $\gamma$ , -1.43and -1.60. Figure 3b plots the measured  $R_s$  versus  $\eta$  for a fixed t = 50 nm and L = 500 and 720 nm. Clearly,  $R_s$  increases monotonically with  $\eta$ . For the L = 500 nm samples, the fitting in Figure 3b gives  $R_{500} = 0.36 \cdot \frac{880 + \eta}{0.98 - \eta} \cdot t^{-1.60}$ . The corresponding  $K'at^y/b = 0.624~\Omega/\square$  is very close to  $R_{\rm T} = 0.761~\Omega/\square$  of the corresponding thin film (t = 50 nm). In addition, if  $\eta$  is set to 0.69, this fitting gives a factor of 1093  $\Omega/\Box$  in front of  $t^{-1.60}$ ,

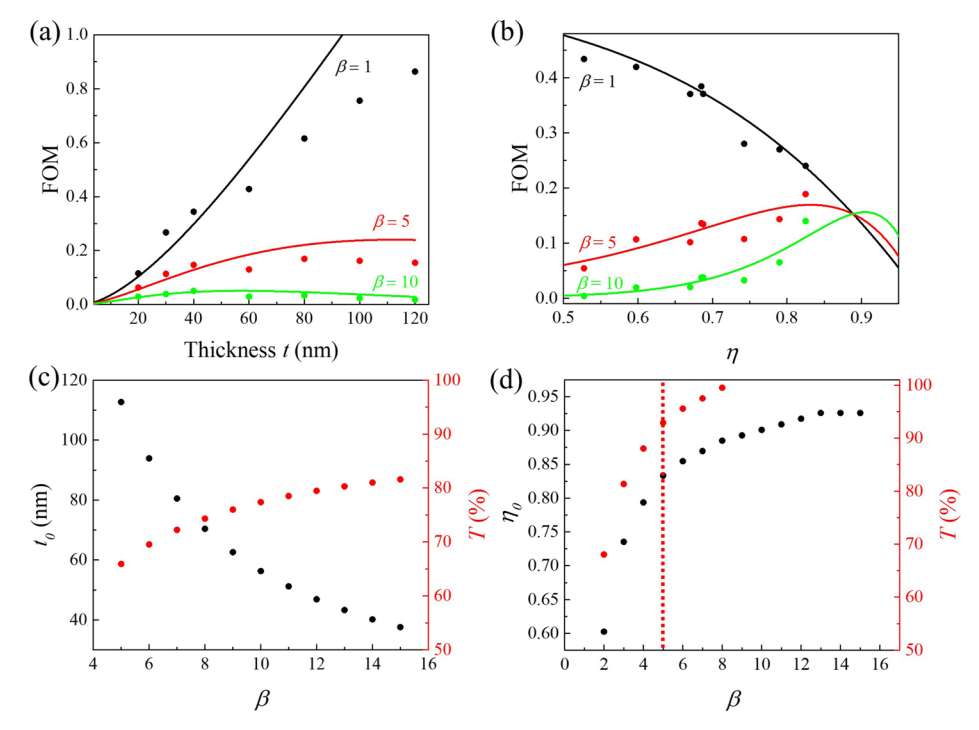


**Figure 5.** (a) Plot of FOM vs t and (b) FOM vs  $\eta$  for Ag NH (L = 500 nm and D = 344 nm) with  $\beta$  = 1 (black), 5 (red), and 10 (green). The colored dots are the experimental data, while the solid curves are plots based on eq 7. The plot of (c) optimal thickness  $t_0$  (eq 8) and (d) optimal  $\eta_0$  (eq 9), where the maximum FOM appears as a function of  $\beta$ .

which is very close to the prefactor 1000  $\Omega/\square$  obtained from the L=500 nm samples in Figure 3a. This indicates that for the L=500 nm samples, both the  $R_{\rm s}$  versus t and  $R_{\rm s}$  versus  $\eta$  data give consistent results. The fitting for the L=720 nm samples gives  $R_{720}=0.12\cdot\frac{1300+\eta}{0.98-\eta}\cdot t^{-1.43}$   $\Omega/\square$  with  $K'at^y/b=0.617$   $\Omega/\square$ . This  $K'at^y/b$  is also similar to  $R_{\rm T}$  (=0.761  $\Omega/\square$ ) of the corresponding thin film. Similarly, the prefactor before  $t^y$  at  $\eta=0.85$  equals to 1115  $\Omega/\square$ , also close to 1360  $\Omega/\square$  obtained from  $R_{\rm s}-t$  fitting for the L=720 nm samples in Figure 3a.

Figure S7 shows the transmission spectra  $T(\lambda)$  of Ag NH structures with different t for L=720 and 500 nm. Similar to the FDTD-calculated results in Figure S4, with the decrease of t, the transmission of the resonance peaks and their spectral widths increase. When t is smaller than 20 nm, the spectral shape changes to a clear transmission dip.  $T_{P_2}$  versus t for t >20 nm with both L = 500 nm, D = 344 nm and L = 720 nm, D= 613 nm is plotted in Figure 3c. For both cases,  $T_{P_2}$  decreases almost linearly with t, similar to the results obtained from FDTD calculations (Figure 2a). The transmission at  $\lambda = 800$ nm for the Ag thin film with the same t is also shown in Figure 3c. The black-dashed curves show the fitting results from eq 6, and good agreements have been achieved. For the L = 720 and 500 nm samples and the thin-film samples, we obtain  $T_{720} = 0.98 \times \mathrm{e}^{-0.0009 \times t}$ ,  $T_{500} = 0.91 \times \mathrm{e}^{-0.0028 \times t}$ , and  $T_{\mathrm{T}} = 0.942 \times \mathrm{e}^{-0.0894 \times t}$ , respectively. For the *D*-dependent  $T(\lambda)$  shown in Figure S8, the transmission of the resonance peaks and their spectral widths decrease with the decrease of D.  $T_{P_2}$  versus  $\eta$ for L = 500 nm and t = 50 nm is plotted in Figure 3d. The dashed curves show the fitting results based on eq 6,  $T_{500}$  =  $(0.86\eta^2 + 0.47) \times e^{-0.0028 \times 50}$ . When  $\eta = 0.69$ , the coefficient before the exponent function equals to 0.88, which is close to

0.91 based on the fitting of the  $T_{500}$ –t relationship from Figure 3c.

Clearly, for both sheet resistance and transmission, good agreements have been observed between the experimental data and the proposed general eqs 3 and 6.

Data from literature studies of various TMFs are also extracted to validate eqs 3 and 6. The fitting results of the resistance model (eq 3) from different TMF structures with different t or  $\eta$  are shown in Figure 4a,b, and the fittings based on eq 6 are presented in Figure 4c,d. The corresponding fitting parameters are listed in Table S1 of the Supporting Information.

Comparing the General Equations and Literature **Results.** There are only few experimental  $R_s$ -t reports in the literature.  $^{37-39}$  The log-log plots of  $R_s$ -t relationship of Au and Ag NHs in Figure 4a clearly show the power law behaviors. As shown in Table S1, the fitting exponent  $\gamma$  of Ag NHs in the literature varies from -1.41 to -3.9, all less than -1, and our experimental values, -1.43 and -1.60, are well within this region. The absolute value of  $\gamma$  reflects how strongly the other phenomena, such as the size, the roughness, and the grain boundary, affect the resistance of the resulting TMFs. The larger the  $|\gamma|$  value, the worse the quality of the TMFs. For example, higher quality of TMFs was achieved for Au NHs as  $0>\gamma>-1$  based on both the experimental results<sup>37</sup> and the FDTD calculations. The huge difference of the  $|\gamma|$  value for Ag and Au TMFs could also be resulted from their intrinsic material difference during the deposition (melting point, adatom surface processes, etc.). Figure 4b shows that eq 3 can fit the  $R_s - \eta$  relationships very well, regardless of materials (Ag<sup>5,11,18</sup> or Cu<sup>4</sup>), structures (ordered<sup>4,5,12,18,34</sup> or random<sup>11</sup>), and even NW networks. 12 The fitting parameter b varies from -0.67 to 1.30, while a changes significantly from -0.17 (which is close to 0) to 890. All these results demonstrate that eq 3 is a good and reasonable empirical model to describe the resistance of any types of TMFs.

The fitting results of T versus t (Figure 4c) and T versus  $\eta$ (Figure 4d) by eq 6 for TMFs with different materials, lattice structures, and networks also show excellent agreements. The t-dependent fitting gives  $\alpha$  ranging from 0.0021 to 0.027 nm<sup>-1</sup>, and most of the  $\alpha$  values stay in between 0.0114 and 0.027 nm<sup>-1</sup>. Our experimental values, 0.0009 and 0.0028 nm<sup>-1</sup>, are significantly smaller than most results obtained in the literature, demonstrating higher optical quality. The  $\eta$ dependence fittings in Figure 4d give the fitting parameters A ranging from 0.80 to 1.66 and B from 0 to 0.36, which are consistent with our experimental results shown in Figure 3d, where A = 0.86 and B = 0.47. In addition, as shown in Figure 4d, except for Cu NH, almost all other transmission data from different Ag TMFs collapse together, following more or less the same function of  $\eta$ .

Thus, in summary, both our own experimental data and data from the literature support the fact that the models for resistance (eq 3) and transmission (eq 6) of TMFs are very effective.

FOM of TMFs. The quality of the TMFs is ultimately determined by their FOMs. The most widely used FOM in the TCF community is the "Haacke" FOM  $\Phi_{\rm H}$  (= $T^{\beta}/R_{\rm s}$ ), as discussed in the Introduction section.<sup>17</sup> For a TCF,  $\beta = 10$ , which is based on Beer-Lambert's law and the simple Ohm's law for a thin film.<sup>17</sup> Such a parameter strongly weights the optical transmission.<sup>21</sup> However, as has been shown previously, for the TMFs, both the resistance and the transmission are functions of  $\eta$  and t, while the resistance follows a power law of t, rather than simply  $t^{-1}$ . Thus,  $\beta = 10$  for  $\Phi_{\rm H}$  is not necessarily the best value to characterize the FOM of the TMFs. Therefore, it is important to determine a more reasonable  $\beta$ value to characterize the FOM of the TMFs.

Based on eqs 3 and 6 as well as the definition of  $\Phi_{H}$ , the FOM of any TMFs can now be expressed as

$$\Phi_{\rm H} = \frac{(b-\eta)[A\eta^2 + B]^{\beta} \cdot e^{-\alpha\beta t}}{K'(a+\eta)t^{\gamma}}$$
(7)

Clearly, the FOM of TMFs is a complex function of t and  $\eta$ . The optimal thickness  $t_o$  and  $\eta_o$  for a TMF where the maximum FOM value appears are determined by  $\frac{\partial \Phi_{H}}{\partial t} = 0$  and  $\frac{\partial \Phi_{\rm H}}{\partial \eta} = 0$ , respectively, which gives the following two equations:  $t_0 = -\gamma/\alpha\beta$  (8)

$$t_{\rm o} = -\gamma/\alpha\beta \tag{8}$$

$$2A\beta\eta_{o}(b-\eta_{o})(\eta_{o}+a) = (a+b)(A\eta_{o}^{2}+B)$$
 (9)

Thus, both  $t_0$  and  $\eta_0$  can be determined independently. For example, based on the fittings on the L = 500 nm samples shown in Figure 3,  $\gamma = -1.60$ ,  $\alpha = 0.0028 \text{ nm}^{-1}$ , a = 880, b =0.98, A=0.86, and B=0.47, we can obtain  $t_{\rm o}=\frac{4000}{7\beta}$  nm, and  $\eta_{o}$ - $\beta$  relationship can be numerically calculated using eq 9.

Figure 5a,b shows the plot of FOM as a function of t and  $\eta$ for Ag NH (L = 500 nm, D = 344 nm) with different  $\beta$ -values (=1, 5, and 10, respectively). The colored dots are the experimental results, while the solid curves are calculated based on eq 7. As shown in Figure 5a,  $\beta = 1$  gives a monotonically increasing relationship between FOM and t when t < 120 nm for both experiments and eq 7, which implies that the maximum FOM occurs at a relatively large film thickness. Such an exponent ( $\beta = 1$ ) weighs FOM too much in favor of  $R_{s}$ , thus resulting in a maximum FOM at a large film thickness (>120 nm) with very low transmission (<65%). A larger  $\beta$  (=5) causes the maximum experimental FOM to appear at  $t_0 = 80$ nm with  $T_{P_2} = 72.4\%$  and  $R_s = 1.17 \ \Omega/\square$ . Equation 7 predicts that  $t_0$  = 112.7 nm with  $T_{P_2}$  = 65.9% and  $R_{\rm s}$  = 0.51  $\Omega/\Box$ , which qualitatively agree with the experimental results. However, if  $\beta$ = 10, the experimental  $t_0$  decreases significantly to 40 nm (about half of the value for  $\beta$  = 5) with  $T_{P_2}$  = 80.77% and  $R_{\rm s}$  = 3.02  $\Omega/\Box$ , that is, the transmission only increases ~11%, while the resistance increases 2.6 times, compared to the  $\beta = 5$  case. A similar trend is observed based on eq 7, with  $t_0 = 57$  nm (half),  $T_{P_3} = 77.18\%$  (17% increment), and  $R_s = 1.55 \Omega/\Box$  (3 times increment). Clearly, when  $\beta$  changes from 5 to 10, a large resistance increase of nearly 3-fold is observed with only <20% transmission increment. The high  $\beta$ -value (=10) weighs FOM too much in favor of *T* for the TMFs. This suggests that  $\beta$  = 5 is a better choice to determine the FOM.

The  $\eta$ -dependent FOM in Figure 5b also demonstrates that  $\beta = 5$  is a better choice for FOM for the TMFs. The following major observations are obtained from Figure 5b: first, all the calculated FOMs based on eq 7 for different  $\beta$ -values match well with the experimental data. Second, a similar trend is observed to that of Figure 5a, that is,  $\beta = 1$  leads to a monotonical decrease of FOM versus  $\eta$  and no  $\eta_0$  is suggested; the experimental FOMs for  $\beta$  = 5 and 10 show a monotonical increase versus  $\eta$ , while the theoretical FOMs based on eq 7 demonstrate an  $\eta_0$  appearing at 0.833 and 0.901, respectively, with  $T_{P_2}$  = 92.7%,  $R_{\rm s}$  = 4.07  $\Omega/\Box$  and  $T_{P_2}\approx$  100%,  $R_{\rm s}$  = 7.56  $\Omega/\square$ . The  $R_s$  value is almost doubled when  $\beta$  increases from 5 to 10, and few transparent conductor applications require more than 90% transmission. Clearly,  $\beta = 5$  gives a better choice to determine the FOM.

To further evaluate the effect of  $\beta$  on  $t_0$  and  $\eta_0$ , Figure 5c,d plots  $t_0$  and  $\eta_0$  versus  $\beta$  based on eqs 8 and 9 as well as the fitting parameters discussed above. The corresponding transmissions are also plotted. Figure 5c shows that with the increase of  $\beta$ ,  $t_0$  decreases dramatically, while  $T_{P_2}$  increases slowly. When  $\beta$  is smaller than 5,  $t_0$  is larger than 120 nm, which is beyond the experimental conditions. When  $\beta$ increases from 5 to 15, t<sub>0</sub> decreases from 112.7 to 37.6 nm, and the corresponding  $T_{P_2}$  and  $R_s$  increase from 65.9% and 0.51  $\Omega/\Box$  to 81.6% and 3.0  $\Omega/\Box$ , respectively. In this case,  $R_{\rm s}$ increases nearly 6-fold, while  $T_{P_2}$  increases only 15%. Thus, selecting a smaller  $\beta$  could better balance the effect of transmission and sheet resistance on the FOM. Figure 5d shows the  $\eta_0$  versus  $\beta$  plot by solving eq 9. In contrast to the  $t_0$ - $\beta$  relationship, with the increase of  $\beta$ ,  $\eta_0$  increases monotonically. When  $\beta$  increases from 2 to 5,  $\eta_0$  increases from 0.602 to 0.833, while the corresponding  $T_{P_2}$  and  $R_{\rm s}$ increase from 68.0% and 1.59  $\Omega/\Box$  to 92.9% and 4.08  $\Omega/\Box$ , respectively. These changes are significant. When  $\beta$  changes from 5 to 15 ( $\beta$  = 5 is marked by the red-dashed line in Figure 5d), the increment of  $\eta_0$  versus  $\beta$  becomes slower, from 0.833 to 0.925, while the  $T_{P_2}$  and  $R_s$  also increase slowly from 92.9% and 4.08  $\Omega/\square$  to  ${\sim}100\%$  and 11.03  $\Omega/\square$  , respectively. The  $R_{\rm s}$ is doubled while the change in  $T_{P_2}$  is only ~7%. Compared to the change in small  $\beta$ -values, these variations are insignificant. In fact, few transparent conductor applications require more than 90% transmission. Thus, it is suggested that  $\beta$  between 2 and 5 could better evaluate the FOM and balance the effect from transmission and sheet resistance. Therefore, based on Figure 5c,d, for the ordered Ag NH TMFs in our report, we select  $\beta = 5$ . For other TMFs, the results from both Figures 4 and 5 also suggest that  $\beta$  would be significantly smaller than 10.

## CONCLUSIONS

In summary, a systematic thickness and PR-dependent study on the Ag NH TMF has been performed, and empirical relationships for resistance and transmission are proposed. The empirical resistance model is based on the network resistor model, the Kirchoff's rules, and the thickness-dependent resistivity, which counts for both the thickness and the PR. The transmission model is based on the effective medium theory, the geometric model, and the Beer-Lambert law. Both models fit well with our systematical experimental data as well as the data reported in the literature, regardless of the lattice structure of the TMFs. Based on these models, a general and comprehensive FOM expression (eq 7) for TMFs is obtained as a function of both film thickness and PR. Both the experimental data and the theoretical predictions show that  $\beta$  = 5 is better to characterize the performance of TMF as compared to  $\beta = 10$  for TCFs. The observed empirical models as well as the FOM expression can be used to characterize any type of TMFs and can be used to assess the overall quality of the TMFs.

#### ASSOCIATED CONTENT

# **Supporting Information**

The Supporting Information is available free of charge at https://pubs.acs.org/doi/10.1021/acs.jpcc.1c04832.

Schematic of the resistors  $R_0$  of the infinite two-dimensional hexagonal resistor lattice and tetragonal resistor lattice,  $T(\lambda)$  of the Ag thin film with different t, FDTD-calculated  $T(\lambda)$  of the Ag NH array with different t (L=500 nm, D=340 nm) and different  $\eta$  (L=500 nm, t=50 nm), SEM images of the Ag NH array with different L and different L and different L of the Ag NH array with different L (L=500 nm, L=340 nm and L=720 nm, L=613 nm), L=500 nm, L=500 nm, L=500 nm, L=500 nm, and fitting results in Figure 4 (PDF)

# AUTHOR INFORMATION

#### **Corresponding Authors**

Zhengjun Zhang — Key Laboratory of Advanced Materials (MOE) and School of Materials Science and Engineering, Tsinghua University, Beijing 100084, P. R. China; orcid.org/0000-0001-8727-6373; Email: zjzhang@tsinghua.edu.cn

Yiping Zhao — Department of Physics and Astronomy, University of Georgia, Athens, Georgia 30602, United States; orcid.org/0000-0002-3710-4159; Email: zhaoy@uga.edu

### **Authors**

Yanfeng Wang — Key Laboratory of Advanced Materials (MOE) and School of Materials Science and Engineering, Tsinghua University, Beijing 100084, P. R. China; Department of Physics and Astronomy, University of Georgia, Athens, Georgia 30602, United States; orcid.org/0000-0001-7698-6230

Fei Yang — Key Laboratory of Advanced Materials (MOE) and School of Materials Science and Engineering, Tsinghua University, Beijing 100084, P. R. China

Complete contact information is available at: https://pubs.acs.org/10.1021/acs.jpcc.1c04832

#### **Author Contributions**

The manuscript was written through contributions of all authors. All authors have given approval to the final version of the manuscript.

## Notes

The authors declare no competing financial interest.

## ACKNOWLEDGMENTS

Y.W., F.Y., and Z.Z. were financially supported by the Basic Science Centre Project of NSFC under grant no. 51788104. Y.Z. was financially supported by the National Science Foundation under Grant no. ECCS-1808271.

## ABBREVIATIONS

TMF,transparent metallic film; TCF,transparent conductive film; PR,perforation area ratio; FOM,figure of merit; MNH,metallic nanohole; NW,nanowire; NSL,nanosphere lithography; EOT,extraordinary optical transmission; SPP,surface plasmon resonance; FDTD,finite difference time domain; FEM,finite element method; PSNS,polystyrene nanosphere; FE-SEM,field-emission scanning electron microscopy

#### REFERENCES

- (1) Li, Z.; Wang, G.; Li, Z.; Cheng, Z.; Zhou, G.; Li, S. Flexible Transparent Electrodes Based on Gold Nanomeshes. *Nanoscale Res. Lett.* **2019**, *14*, 132.
- (2) Qiu, T.; Akinoglu, E. M.; Luo, B.; Giersig, M.; Liang, M.; Ning, J.; Zhi, L. Shape Control of Periodic Metallic Nanostructures for Transparent Conductive Films. *Part. Part. Syst. Charact.* **2017**, *34*, 1600262.
- (3) Bao, C.; Yang, J.; Gao, H.; Li, F.; Yao, Y.; Yang, B.; Fu, G.; Zhou, X.; Yu, T.; Qin, Y. In Situ Fabrication of Highly Conductive Metal Nanowire Networks with High Transmittance from Deep-Ultraviolet to near-Infrared. *ACS Nano* **2015**, *9*, 2502–2509.
- (4) Wang, Q.; Raglione, M.; Li, B.; Jin, X.; Toor, F.; Arnold, M.; Ding, H. High Throughput Laser Process of Transparent Conducting Surfaces for Terahertz Bandpass Ultrathin Metamaterials. *Sci. Rep.* **2019**, *9*, 3083.
- (5) Ho, Y.-H.; Chen, K.-Y.; Liu, S.-W.; Chang, Y.-T.; Huang, D.-W.; Wei, P.-K. Transparent and Conductive Metallic Electrodes Fabricated by Using Nanosphere Lithography. *Org. Electron.* **2011**, 12, 961–965.
- (6) Qiu, T.; Luo, B.; Akinoglu, E. M.; Yun, J. H.; Gentle, I. R.; Wang, L. Trilayer Nanomesh Films with Tunable Wettability as Highly Transparent, Flexible, and Recyclable Electrodes. *Adv. Funct. Mater.* **2020**, *30*, 2002556.
- (7) Wu, W.; Tassi, N. G. A Broadband Plasmonic Enhanced Transparent Conductor. *Nanoscale* **2014**, *6*, 7811–7816.
- (8) Siddall, G.; Tellier, C. R.; Tosser, A. J. Size Effects in Thin Films; Elsevier: Amsterdam, 1982.
- (9) Liu, H.-D.; Zhao, Y.-P.; Ramanath, G.; Murarka, S. P.; Wang, G.-C. Thickness Dependent Electrical Resistivity of Ultrathin (<40 Nm) Cu Films. *Thin Solid Films* **2001**, 384, 151–156.
- (10) Li, M.; Zhao, Y.-P.; Wang, G.-C. In Situ Measurement of Thickness Dependent Electrical Resistance of Ultrathin Co Films. *J. Vac. Sci. Technol., A* **2000**, *18*, 2992–2996.
- (11) Reilly, T. H.; Tenent, R. C. Controlling the Optical Properties of Plasmonic Disordered Nanohole Silver Films. *ACS Nano* **2010**, *4*, 615–624.

- (12) van de Groep, J.; Spinelli, P.; Polman, A. Transparent Conducting Silver Nanowire Networks. *Nano Lett.* **2012**, *12*, 3138–3144.
- (13) Choy, T. C. Effective Medium Theory: Principles and Applications, 2nd ed.; Oxfrod University Press: Great Clarendon Sreet: Oxford, OX2 6DP, United Kingdom, 2016.
- (14) Wang, Y.; Luong, H.; Zhang, Ž.; Zhao, Y. Coupling between Plasmonic Nanohole Array and Nanorod Arrays: The Emerging of a New Extraordinary Optical Transmission Mode and Epsilon-near-Zero Property. J. Phys. D: Appl. Phys. 2020, 53, 275202.
- (15) Ghaemi, H. F.; Thio, T.; Grupp, D. E. Surface Plasmons Enhance Optical Transmission through Subwavelength Holes. *Phys. Rev. B: Condens. Matter Mater. Phys.* **1998**, *58*, 6779–6782.
- (16) Wang, Y.; Zhang, Z.; Zhao, Y. The Effect of Nanorod Position on the Plasmonic Properties of the Complex Nanorod in Nanohole Arrays. J. Phys. D: Appl. Phys. 2021, 54, 155201.
- (17) Haacke, G. New Figure of Merit for Transparent Conductors. J. Appl. Phys. 1976, 47, 4086–4089.
- (18) Morfa, A. J.; Akinoglu, E. M.; Subbiah, J.; Giersig, M.; Mulvaney, P. Transparent Metal Electrodes from Ordered Nanosphere Arrays. *J. Appl. Phys.* **2013**, *114*, 054502.
- (19) Torrisi, G.; Luis, J. S.; Sanchez-Sobrado, O.; Raciti, R.; Mendes, M. J.; Águas, H.; Fortunato, E.; Martins, R.; Terrasi, A. Colloidal-Structured Metallic Micro-Grids: High Performance Transparent Electrodes in the Red and Infrared Range. *Sol. Energy Mater. Sol. Cells* **2019**, 197, 7–12.
- (20) Sannicolo, T.; Lagrange, M.; Cabos, A.; Celle, C.; Simonato, J. P.; Bellet, D. Metallic Nanowire-Based Transparent Electrodes for Next Generation Flexible Devices: A Review. *Small* **2016**, *12*, 6052–6075.
- (21) Barnes, T. M.; Reese, M. O.; Bergeson, J. D.; Larsen, B. A.; Blackburn, J. L.; Beard, M. C.; Bult, J.; van de Lagemaat, J. Comparing the Fundamental Physics and Device Performance of Transparent, Conductive Nanostructured Networks with Conventional Transparent Conducting Oxides. *Adv. Energy Mater.* **2012**, *2*, 353–360.
- (22) Skehan, C.; Ai, B.; Larson, S. R.; Stone, K. M.; Dennis, W. M.; Zhao, Y. Plasmonic and SERS Performances of Compound Nanohole Arrays Fabricated by Shadow Sphere Lithography. *Nanotechnology* **2018**, *29*, 095301.
- (23) Ai, B.; Song, C.; Bradley, L.; Zhao, Y. Strong Fano Resonance Excited in an Array of Nanoparticle-in-Ring Nanostructures for Dual Plasmonic Sensor Applications. *J. Phys. Chem. C* **2018**, *122*, 20935—20944.
- (24) Wang, Y.; Chong, H. B.; Zhang, Z.; Zhao, Y. Large-Area Fabrication of Complex Nanohole Arrays with Highly Tunable Plasmonic Properties. *ACS Appl. Mater. Interfaces* **2020**, *12*, 37435—37443.
- (25) Ai, B.; Luong, H. M.; Zhao, Y. Chiral Nanohole Arrays. *Nanoscale* **2020**, *12*, 2479–2491.
- (26) Ingram, W. M.; Han, C.; Zhang, Q.; Zhao, Y. Optimization of Ag-Coated Polystyrene Nanosphere Substrates for Quantitative Surface-Enhanced Raman Spectroscopy Analysis. *J. Phys. Chem. C* **2015**, *119*, 27639–27648.
- (27) Larsen, G. K.; He, Y.; Ingram, W.; Zhao, Y. Hidden Chirality in Superficially Racemic Patchy Silver Films. *Nano Lett.* **2013**, *13*, 6228–6232.
- (28) He, Y.; Larsen, G. K.; Ingram, W.; Zhao, Y. Tunable Three-Dimensional Helically Stacked Plasmonic Layers on Nanosphere Monolayers. *Nano Lett.* **2014**, *14*, 1976–1981.
- (29) Palik, E. D. *Handbook of Optical Constants of Solids*; Academic Press: Orlando, FL, 1985.
- (30) Atkinson, D.; van Steenwijk, F. J. Infinite Resistive Lattices. *Am. J. Phys.* **1999**, *67*, 486–492.
- (31) Cserti, J. Application of the Lattice Green's Function for Calculating the Resistance of an Infinite Network of Resistors. *Am. J. Phys.* **2000**, *68*, 896–906.
- (32) Ding, G.; Clavero, C.; Schweigert, D.; Le, M. Thickness and Microstructure Effects in the Optical and Electrical Properties of Silver Thin Films. *AIP Adv.* **2015**, *5*, 117234.

- (33) Sondheimer, E. H. The Mean Free Path of Electrons in Metals. *Adv. Phys.* **1952**, *1*, 1–42.
- (34) Theuring, M.; Steenhoff, V.; Geissendorfer, S.; Vehse, M.; von Maydell, K.; Agert, C. Laser Perforated Ultrathin Metal Films for Transparent Electrode Applications. *Opt. Express* **2015**, *23*, A254–A262
- (35) Ebbesen, T. W.; Lezec, H. J.; Ghaemi, H. F.; Thio, T.; Wolff, P. A. Extraordinary Optical Transmission through Sub-Wavelength Hole Arrays. *Nature* **1998**, *391*, *667*–*669*.
- (36) Kang, E. S. H.; Ekinge, H.; Jonsson, M. P. Plasmonic Fanoholes: On the Gradual Transition from Suppressed to Enhanced Optical Transmission through Nanohole Arrays in Metal Films of Increasing Film Thickness. *Opt. Mater. Express* **2019**, *9*, 1404–1415.
- (37) Cheng, K.; Cui, Z.; Li, Q.; Wang, S.; Du, Z. Large-Scale Fabrication of a Continuous Gold Network for Use as a Transparent Conductive Electrode in Photo-Electronic Devices. *Nanotechnology* **2012**, *23*, 425303.
- (38) Qiu, T.; Luo, B.; Ali, F.; Jaatinen, E.; Wang, L.; Wang, H. Metallic Nanomesh with Disordered Dual-Size Apertures as Wide-Viewing-Angle Transparent Conductive Electrode. *ACS Appl. Mater. Interfaces* **2016**, *8*, 22768–22773.
- (39) Chen, X.; He, Y.; Chen, X.; Huang, C.; Li, Y.; Cui, Y.; Yuan, C.; Ge, H. Non-Iridescent Metal Nanomesh with Disordered Nanoapertures Fabricated by Phase Separation Lithography of Polymer Blend as Transparent Conductive Film. *Materials* **2021**, *14*, 867.
- (40) Hajiaboli, A.; Kahrizi, M.; Truong, V.-V. Optical Behaviour of Thick Gold and Silver Films with Periodic Circular Nanohole Arrays. *J. Phys. D: Appl. Phys.* **2012**, *45*, 485105.